## Chemical routes to materials

# Effect of Cu substitution on magnetic and photocatalytic properties of Mn–ZnFe$_2$O$_4$ nanoparticles

N. I. Abu-Elsaad[1,*] and A. S. Nawara[1]

[1] *Magnetic Semiconductor Laboratory, Physics Department, Faculty of Science, Zagazig University, Zagazig, Egypt*

## ABSTRACT

The citrate approach was employed to successfully synthesize Mn$_{0.4}$Zn$_{0.6-x}$Cu$_x$Fe$_2$O$_4$ (MZCF) with a nanostructured shape. A thorough examination was conducted on the microstructural, magnetic, and optical properties of the nanoparticles obtained. The X-ray diffraction (XRD) patterns revealed that all of the compositions exhibit a high degree of single-phase spinel formation. The experimental findings indicate that the introduction of copper ions leads to a reduction in both lattice constant and porosity, while concurrently resulting in an increase in the theoretical X-ray and bulk densities. The analysis of UV–Vis spectroscopy indicated that MZCF exhibited a direct band gap falling within the range of 1.61–1.78 eV. The magnetic characteristics were assessed through the analysis of hysteresis plots. The introduction of copper (Cu) content leads to notable improvements in the saturation ($M_s$) and remanent magnetization ($M_r$) values, which range from 40.21 to 58.78 and 4.46–10.54 emu/g, respectively. The assessment of the microwave frequency response has verified the appropriateness of MZCF nanoferrites for application within the frequency spectrum spanning from 8 to 13 gigahertz. The nanoparticles exhibit improved magnetic properties, suggesting their potential appropriateness for applications involving high-frequency microwave absorption and switching. Furthermore, the nanoparticles Mn$_{0.4}$Zn$_{0.6}$Fe$_2$O$_4$ and Mn$_{0.4}$Zn$_{0.2}$Cu$_{0.4}$Fe$_2$O$_4$ were subjected to analysis utilizing a solar light simulator in order to induce degradation of MB dye.

## Introduction

Due to its technological relevance, nanomaterials science has garnered considerable research interest in both the past and present, seeing rapid growth. The area of technology has seen a significant advancement in the creation of ferrites, owing to the improvement in synthesis and characterization methods at the nanoscale. Nanocrystalline spinel ferrites, characterized by the basic structure MFe$_2$O$_4$ (where M, including but not limited to Co, Mn, Ni, Zn, and Cu), exhibit considerable intrigue as magnetic materials due to

---

their diverse range of uses and scientific implications [1]. The significance of magnetic materials stems from their extensive array of benefits and the many compositional replacements included into ferrites, resulting in enhanced physical characteristics. Since their crystalline size is on the nanoscale, magnetic nanoparticles (MNPs) exhibit remarkable characteristics [2]. Currently, MNPs are a burgeoning area of study among academics because of its wide-ranging uses stemming from its distinct characteristics in several domains. The collective utilization of these MNPs has mostly focused on advancing magnetic sensors for the electronics and energy sectors, data storage, magnetic fluids, environmental cleanup, electronic communication, biomedicine, and other related fields [3]. The progress in artificial medical science study has been propelled by the emergence of the MNPs field, which is utilized for medication administration, MRI screenings, and hyperthermia therapies. Manganese–zinc (Mn–Zn) ferrites are preferred over other ferrite materials owing to their advantageous characteristics, including a high saturation magnetization, favorable initial permeability, and low residual magnetization. These characteristics make them well-suited for technological applications requiring minimal losses [4].

Altering ions and magnetic spins throughout the lattice sites resulted in the deliberate modification of the physical characteristics [5]. The spinel structure is categorized by the presence of two lattice sites, namely A and B sites. It is observed that $M^{2+}$ cations tend to inhabit the A site, whereas trivalent cations preferentially occupy the B-site [6]. In ferrites, the exchange interaction is facilitated by super-exchange interaction involving oxygen ions. This is due to the relatively large size of the cations, which prevents them from directly interacting with each other. It is seen that the AB interaction exhibits a significant dominance over the AA and BB interactions in three distinct exchange interactions. Within the A site, the magnetic spins demonstrate a unidirectional alignment, whereas at the B site, they exhibit an opposite alignment, leading to an interaction among the A and B sites. Thus, inside the AB interaction, two sub-lattices that are saturated and magnetized are formed at absolute zero temperature. Hence, the net magnetization of the lattice can be characterized as the disparity in magnetization values between the B- and A-sublattices. Several techniques are employed to synthesize spinel ferrites, such as the sol–gel autocombustion (SGAC) process [7, 8], glass method [9], solid state approach [10], co-precipitation

technique [11], and the microwave method [12]. The SGAC approach was determined to be superior as a result of its low-temperature preparation, which leads to improved particle homogeneity, refined surface morphology, and exceptional characteristics [13].

Recently, the problem of water, in conjunction with food and energy, has been widely recognized as a significant concern in contemporary society [14]. Water pollution is a pressing concern that poses a considerable danger to the ecological well-being of many living organisms within a given community [15]. Numerous heavy metals, possessing potential damage, are transported through diverse ways across distinct areas. The escalating global population, along with the rapid pace of modernization and manufacturing, has emerged as the predominant catalysts for water pollution [16]. Nanoferrites have emerged as a highly promising class of photocatalysts due to their narrow band gap, exceptional stability, favorable adsorption capabilities, cost-effectiveness, ease of regeneration, environmental compatibility, and relatively small band gap of 2.0 eV. These attributes render them highly suitable for facilitating photocatalytic processes [17]. The existing research frame provides evidence that ferrites can facilitate the degradation of several kinds of dyes [18–21].

Based on the currently available knowledge, there is a scarcity of accessible publications related to $Cu^{2+}$-doped MZF nanoparticles (NPs). In the present investigation, we explain in detail the MZCF NPs synthesis procedure. Additionally, we examine the microstructural, magnetic, optical characteristics, and photocatalytic efficacy of the MZCF NPs regarding MB dye.

## Experimental procedure

$Mn_{0.4}Zn_{0.6-x}Cu_xFe_2O_4$ NPs with varying amounts of copper ions ($Cu^{2+}$) ($x = 0$, 0.1, 0.2, 0.3, and 0.4) were formed using the citrate process. The chemicals used in the experiment were metals nitrates, citric acid, and ammonia solution. In distilled water, the citric acid and metal nitrates were dissolved in stoichiometric quantities to produce a homogenous solution. The procedure was sped up by introducing an ammonia solution to get the pH to a neutral 7. The obtained solution was heated at a temperature of 100 °C while being continuously stirred, leading to the precipitation of the solution and its transformation into a viscous

gel. Upon reaching a temperature of 350 °C, the desiccated gel underwent ignition, resulting in self-sustaining burning and the subsequent formation of ash composed of ferrite nano-powder.

XRD patterns were obtained by measuring the $2\theta$ angles within the range of 20° to 80°. This was achieved by Cu K radiation ($\lambda = 1.54056$ Å) employing a Philips X'Pert diffractometer. The microstructure of the produced NPs was examined by a TEM (JEOL JEM-2100). The diffuse reflectance spectrophotometer (JASCO V-570) was utilized to test the optical characteristics. The synthesized compounds were tested in a Lakeshore 7410 vibrating sample magnetometer (VSM) for their magnetic characteristics at 300 K. The experimental procedure involved the application of a magnetic field within a range of − 20 to 20 kG.

The photocatalytic efficiency of $Mn_{0.4}Zn_{0.6-x}Cu_xFe_2O_4$ photocatalysts, with x values of 0 and 0.4, was assessed by evaluating the degradation of MB during visible light exposure. The experiment was performed using a 100 ml of MB, which was prepared by diluting it with distilled water. In every reaction suspension, 150 mg of the sample was introduced into a 100 ml MB (0.01 g L$^{-1}$). The suspension was allowed to remain in the dark for 1 h while being vigorously stirred, to achieve adsorption–desorption equilibrium among the dye and photocatalyst. Subsequently, the solution was subjected to visible light illumination using a 300-W Xenon lamp. In the process of lighting, continuous stirring was used to ensure the homogeneous distribution of the mixture. A measure 3 mL was taken from the methylene blue solution at different times and the absorbance of MB was collected by UV–visible spectroscopy.

## Results and discussion

### XRD analysis

Figure 1 presents the X-ray diffractograms of MZCF NPs. The confirmation of crystallinity in all the synthesized nanoparticles was achieved by the observation of strong and sharp peaks, which were identified by their respective Miller indices, including (111), (220), (311), (222), (400), (422), (511), (440), (620), and (533). Copper ions appear to have been effectively replaced into the crystalline structure of MZ nanoferrites, since no secondary phase was seen. The observed peaks exhibit a high level of concordance with the PDF card
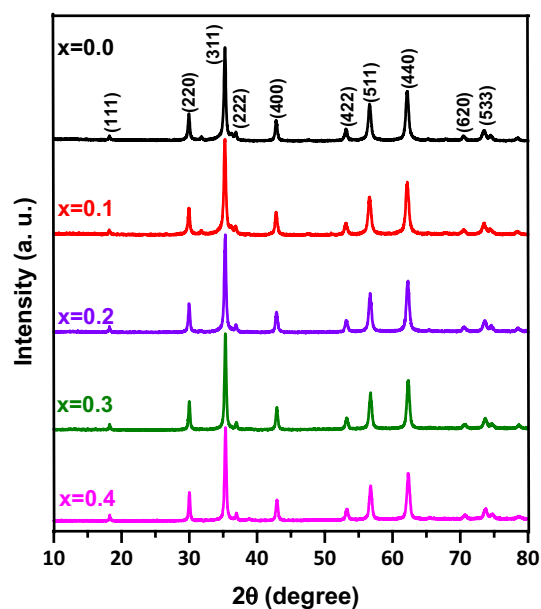


**Figure 1** X-ray diffraction patterns of MZC nanoferrites.

#01-081-8895. The inset in Fig. 1 illustrates the little displacement of the (311) reflection peak to a greater $2\theta$ angle when Cu ions are substituted. This result implies a reduction in the size of the unit cell lattice, indicating the full dissolution of copper ions inside the original lattice structure. The lattice constant 'a' is determined using the Rietveld refinement technique implemented using the MAUD program, the refinement parameters are displayed Table 1. Figure 2 displays the XRD pattern of the $Mn_{0.4}Zn_{0.6-x}Cu_xFe_2O_4$ (x = 0.0, 0.2, and 0.4), which has been subjected to refinement using the Rietveld method. The findings indicate a minimal or negligible disparity between the observed and predicted peaks. The lattice constants for all the specimens are computed and displayed in Table 1. The observed trend is shown in Fig. 3; when Cu doping is increased from 0 to 0.4, the lattice parameter falls from 8.454 to 8.435 Å. This value is reduced because $Zn^{2+}$ ions are replaced with $Cu^{2+}$ ions, which have a lesser ionic radius of (0.73 Å) than $Zn^{2+}$ ions (0.80 Å). When Cu ions are injected into the ferrite lattice, other research groups have seen a similar alteration in the lattice constant [22–24].

The sizes of the crystallites ($t_{Sch}$) are determined for all the specimens using Scherrer's equation [25]:

$$t_{Sch} = \frac{K\lambda}{\beta \cos \theta} \tag{1}$$

**Table 1** Rietveld refinements parameters, lattice parameter (a), crystallite size (t), and microstrain (ε) for MZCF nanoparticles

| x | Rwp (%) | Rb (%) | Rexp (%) | $a$ (Å) | $t_{Sch}$ (nm) | $t_{WH}$ (nm) | $\varepsilon$ ($10^{-4}$) |
|---|---------|--------|----------|---------|----------------|---------------|---------------------------|
| 0.0 | 16.88 | 19.11 | 0.39 | 8.454 | 43.67 | 67.63 | 6.89 |
| 0.1 | 17.87 | 19.25 | 0.39 | 8.453 | 40.53 | 51.16 | 5.23 |
| 0.2 | 14.26 | 15.75 | 0.35 | 8.444 | 42.81 | 63.31 | 8.22 |
| 0.3 | 12.79 | 13.83 | 0.31 | 8.437 | 44.9 | 77.89 | 7.85 |
| 0.4 | 12.12 | 12.24 | 0.30 | 8.435 | 46.71 | 81.56 | 12.1 |
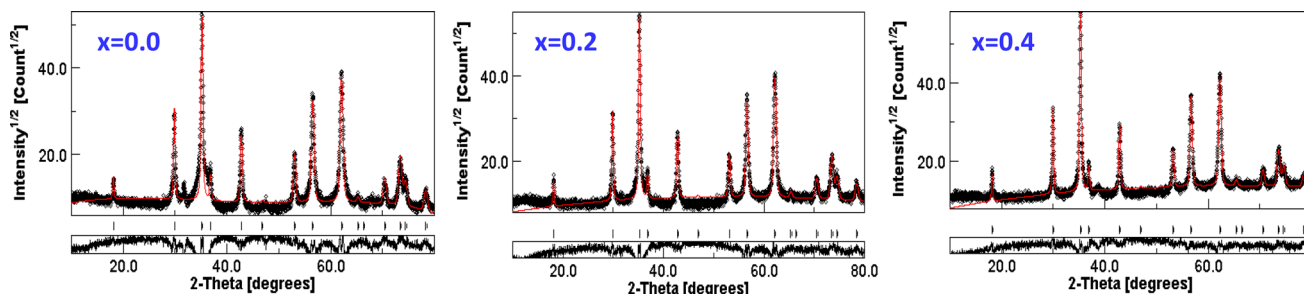


**Figure 2** Rietveld refined XRD patterns of $Mn_{0.4}Zn_{0.6-x}Cu_x Fe_2O_4$ ($x = 0.0$, 0.2, and 0.4) NPs.
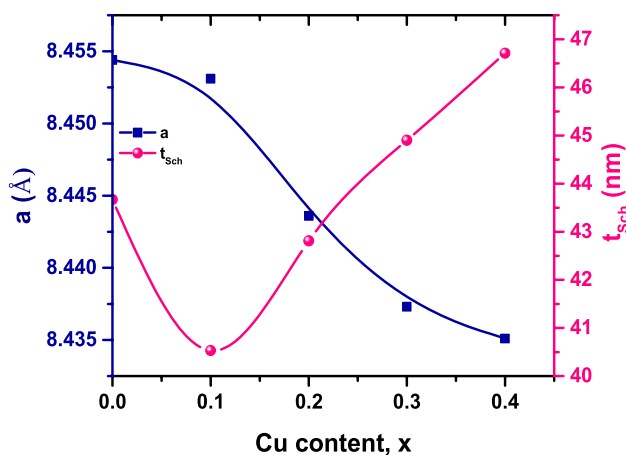


**Figure 3** Plot of lattice constant and crystallite size versus $Cu^{2+}$ concentration for MZC nanoferrites.

In this context, '$\theta$,' '$K$,' '$\lambda$,' and '$\beta$' have their usual meaning. The sizes of all samples are documented in Table 1. Figure 3 indicates that for lower Cu concentrations ($x = 0.1$), there was a decrease in $t_{Sch}$. However, with Cu concentrations ≥ 0.2, the crystallite size exhibited a rising trend. Nevertheless, there is an observed growth in the size of the crystallites, despite the fact that the ionic radius of $Cu^{2+}$ is smaller than that of $Zn^{2+}$. The observed rise in crystallite size in the MZCF system can be attributed to the expansion of ferrite materials when the concentration of $Cu^{2+}$ ions increases. The increase in Cu content leads to

the growth of grains due to the production of a liquid phase during the synthesis process. The presence of this liquid phase enhances the mobility of atoms, hence facilitating grain growth. By augmenting the Cu concentration in the sample, the quantity of liquid phase in the manufacturing procedure escalates, leading to the enlargement of the crystallite size [26]. A further explanation of these mechanisms will be provided in the subsequent section.

While Scherrer's method is effective in determining the average crystallite size, it is important to place greater emphasis on the strain that arises from the exchange of $Zn^{2+}$ ions with $Cu^{2+}$ ions. The discrepancy in the ionic radii between the dopant and the host element gives rise to lattice imperfections and distortions, leading to the production of strain. Williamson–Hall (W–H) equation is investigated to carry out strain analysis [27]:

$$\beta \cos \theta = 4\varepsilon \sin \theta + \frac{K\lambda}{t_{WH}} \qquad (2)$$

Determining strain involves assessing the slope of the linear regression line that is constructed using the variables $\beta\cos\theta$ and $4\sin\theta$. The estimated values resulting from this analysis are provided in Table 1. Figure 4 depicts the Williamson Hall figure for MZCF NPs, where $x = 0$, 0.1, 0.3, and 0.4. Materials are assumed to be isotropic if the strain is the same in all directions relative to the crystallographic axes,
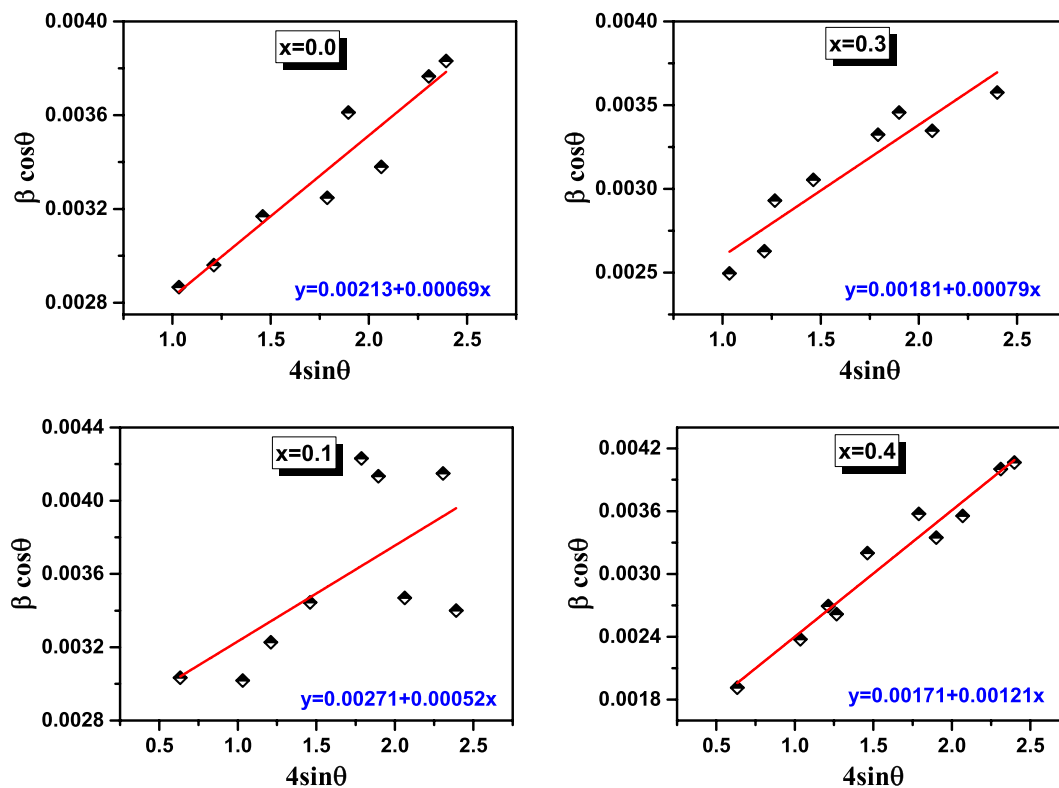
**Figure 4** W–H plot for $Mn_{0.4}Zn_{0.6-x}Cu_x Fe_2O_4$ ($x = 0.0$, 0.1, 0.3 and 0.4).

as is the case with the uniform deformation model, which is linked to the W–H equation. Based on our research findings, it has been seen that there is a significant amount of scattering among the data points in the $\beta\cos\theta$ vs. $4\sin\theta$ graph for sample $x = 0.1$. This suggests that there is an uneven distribution of strain along the crystallographic axes in the synthesized specimen. Table 1 presents a comparison examination whereby the crystallite size determined by the Scherrer approach is shown to be less than the size derived using the W–H plots. This discrepancy arises because the W–H plots take into account the separation of the broadening of the peaks caused by both size and strain factors. In contrast, the observed rise in the micro strain constant for $Mn_{0.4}Zn_{0.4}Cu_{0.2}Fe_2O_4$, $Mn_{0.4}Zn_{0.3}Cu_{0.3}Fe_2O_4$, and $Mn_{0.4}Zn_{0.2}Cu_{0.4}Fe_2O_4$ ferrites, in comparison with $Mn_{0.4}Zn_{0.6}Fe_2O_4$, might be credited to the occurrence of $Cu^{2+}$ ions that occupy octahedral lattice positions. A negative slope implies the existence of compressive strain, whereas a positive slope reveals the potential for tensile strain [28]. The current investigation observed a positive slope in the case of pure $Mn_{0.4}Zn_{0.6}Fe_2O_4$ and doped $Mn_{0.4}Zn_{0.6-x}Cu_xFe_2O_4$, indicating the existence of

tensile strain. It is also verified that these MZCF NPs exhibit brittleness.

The X-ray density of the produced MZCF NPs is evaluated based on the XRD data, employing the subsequent relationship [25]:

$$d_x = \frac{8M_{wt}}{N_A a^3} \tag{3}$$

The symbol $N_A$ denotes Avogadro's number, whereas $M_{wt}$ indicates the molecular weight. The X-ray density results exhibit an increment with Cu addition, as seen in Fig. 5. The observed phenomena can be assigned to a lowering in lattice constant as the concentration of $Cu^{2+}$ ions rises. The increased density of $Cu^{2+}$ ions (8.92 g/cm³) in comparison with $Zn^{2+}$ ions (7.14 g/cm³) may cause the observed increase. In addition, the determination of bulk density ($d_b$) for the manufactured MZCF samples involved the utilization of the mass (m), radius (r), and thickness (h) measurements of the pellet specimens:

$$d_b = \frac{m}{\pi r^2 h} \tag{4}$$
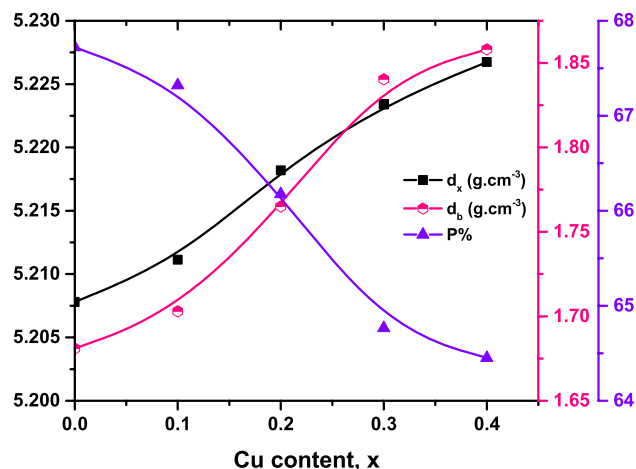
**Figure 5** Graphical representation of $d_x$, $d_B$, and P% of MZCF NPs.

Figure 5 illustrates the observed variance in bulk density ($d_b$) across different compositions. The observed discrepancy between the $d_b$ and $d_x$ can be attributed to pores forming during the preparation procedure. The percentage porosity ($P\%$) for the MZCF NPs was evaluated, as shown in the formula provided below [29]:

$$P\% = 100\left(1 - \frac{d_b}{d_x}\right) \quad (5)$$

The observed trend indicates a decline in the percentage porosity, particularly from 67.24 to 64.45%, as the Cu concentration in the samples increases (Fig. 5). The observed phenomenon can be attributed to an augmentation in the density and a variation in the crystallite size [30].

## Calculation of ionic radii and bond length:

The ionic radii values of MZCF samples have been determined by the use of the following formulae [29]:

$$r_A = \left(u - \frac{1}{4}\right)a\sqrt{3} - R_o \quad (6)$$

$$r_B = \left(\frac{5}{8} - u\right)a - R_o \quad (7)$$

The oxygen location parameter is u ($\sim 0.381$ Å), while the oxygen ion radius is $R_o$ (1.32 Å). When Cu ions were co-doped into the MZF nanoparticles, the site radii ($r_A$ and $r_B$) shrank slightly. This effect is caused by the

**Table 2** Internal structural parameters and values of interionic distances ($p$, $q$, $r$, $s$, $b$, $c$, $d$, $e$, $f$) of $Mn_{0.4}Zn_{0.6-x}Cu_x Fe_2O_4$ ($x=0.0, 0.1, 0.2, 0.3,$ and 0.4) NPs

| Parameters | $x=0.0$ | $x=0.1$ | $x=0.2$ | $x=0.3$ | $x=0.4$ |
|---|---|---|---|---|---|
| $r_A$ | 0.5982 | 0.5973 | 0.5959 | 0.5948 | 0.5939 |
| $r_B$ | 0.7428 | 0.7418 | 0.7403 | 0.7391 | 0.7381 |
| $L_A$ | 1.9182 | 1.9173 | 1.9159 | 1.9148 | 1.9139 |
| $L_B$ | 2.0640 | 2.0631 | 2.0616 | 2.0604 | 2.0594 |
| $L_{AE}$ | 3.1324 | 3.1309 | 3.1287 | 3.1269 | 3.1254 |
| $L_{BE}$ | 2.8455 | 2.8441 | 2.8421 | 2.8404 | 2.8391 |
| $L_{BUE}$ | 2.9907 | 2.9893 | 2.9871 | 2.9854 | 2.9839 |
| $p$ | 2.0628 | 2.0618 | 2.0603 | 2.0591 | 2.0581 |
| $q$ | 1.9182 | 1.9173 | 1.9159 | 1.9148 | 1.9139 |
| $r$ | 3.6731 | 3.6713 | 3.6687 | 3.6666 | 3.6648 |
| s | 3.6899 | 3.6882 | 3.6856 | 3.6834 | 3.6817 |
| $b$ | 2.9889 | 2.9875 | 2.9854 | 2.9836 | 2.9822 |
| $c$ | 3.5048 | 3.5032 | 3.5007 | 3.4986 | 3.4969 |
| $d$ | 3.6607 | 3.6589 | 3.6564 | 3.6542 | 3.6525 |
| $e$ | 5.4910 | 5.4884 | 5.4845 | 5.4813 | 5.4787 |
| $f$ | 5.177 | 5.1746 | 5.1709 | 5.1678 | 5.1654 |

decreased ionic radius of $Cu^{2+}$ ions, which replace $Zn^{2+}$ ions. Previously, it has been observed a similar tends of site radii ($r_A$ and $r_B$) [23, 28].

Using the provided relations [31], we can get the tetrahedral bond length '$L_A$' and the octahedral bond length '$L_B$';

$$L_A = \sqrt{3}a\left(\Delta + \frac{1}{8}\right) \quad (8)$$

$$L_B = a\left(3\Delta^2 - \frac{\Delta}{2} + \frac{1}{16}\right)^{1/2} \quad (9)$$

where $\Delta$ represents the deviation factor from the ideal u, with $\Delta$ calculated as (u − 0.375). The results (Table 2) exhibit a downward trend as the concentration of $Cu^{2+}$ increases, which aligns with the observed changes in the lattice constant.

The equations used in the determination of shared '$L_{AE}$ and $L_{BE}$' and unshared '$L_{BUE}$' edges in spinel ferrite NPs are as follows [31]:

$$L_{AE} = \sqrt{2}a\left(2u - \frac{1}{2}\right) \quad (10)$$

$$L_{BE} = \sqrt{2}a(1 - 2u) \quad (11)$$

$$L_{BUE} = a\left(4u^2 - 3u + \frac{11}{16}\right)^{1/2} \qquad (12)$$

The results of the structural parameter calculations for the $A$ and $B$ sites are displayed in Table 2. The decrease in shared and unshared edge values as the content of $Cu^{2+}$ increases can be clarified by the comparatively smaller atomic radius of $Cu^{2+}$ in comparison with $Zn^{2+}$. Additionally, it should be noted that these variables exhibit a dependency on the lattice constant, which experiences a drop due to $Cu^{2+}$-substitution. A reduction in lattice constant results in a decrease in shared and unshared edge magnitudes.

## Inter-ionic distances

The 'distances between ions,' i.e., '[cations–anions]' and '[cations–cations]' were inferred based on the relationships below [32];

Me – O     Me – Me

$$p = a\left(\frac{5}{8} - u\right) \quad b = \left(\frac{a}{4}\right)2^{1/2}$$

$$q = a\left(u - \frac{1}{4}\right)3^{1/2} \quad c = \left(\frac{a}{8}\right)11^{1/2}$$

$$r = a\left(u - \frac{1}{8}\right)11^{1/2} \quad d = \left(\frac{a}{4}\right)3^{1/2}$$

$$s = a\left(\frac{u}{3} + \frac{1}{8}\right)3^{1/2} \quad e = \left(\frac{3a}{8}\right)3^{1/2}$$

$$f = \left(\frac{a}{4}\right)6^{1/2}$$

Table 2 illustrates the progressive decrease in interionic distances resulting from the incremental inclusion of $Cu^{2+}$ ions. Moreover, it is evidence that the 'interionic distances' exhibit a progressive reduction as the quantity of $Cu^{2+}$ ion doping increases. The decrease in inter-ionic distances is readily apparent since these lengths are directly influenced by the values of the lattice constants [28, 33].

## Morphological analysis

HR-TEM was used to conduct a more detailed analysis of the distinct distribution of particle sizes, aggregation, and lattice planes of the synthesized NPs. The TEM pictures of $Mn_{0.4}Zn_{0.6-x}Cu_xFe_2O_4$ (where $x = 0.0$ and 0.2) are exhibited in Fig. 6a–b. The presented photographs indicate that a significant portion of the particles have a homogeneous composition characterized by substantial agglomeration with a spongy structure. This phenomenon might be explained by magnetic interactions between nanoparticles having a large surface area. The micrographs illustrate that most particles exhibit a nanoscale size and assume a roughly spherical morphology. Particle sizes varied somewhat, although this was confirmed by the size histograms. The average particle size is ~ 24.05 nm ($x = 0.0$) and ~ 26 nm ($x = 0.2$), which is comparable with the crystallite size reported by XRD examination. The estimated values obtained from X-ray data using the Scherrer formula are slightly smaller, measuring 43 and 42 nm, whereas the values obtained using the Williamson–Hall equation are 67 and 63 nm. The discrepancy in those values can be ascribed to the assumption of spherical particle shape, which was utilized in the application of the Scherrer formula and Williamson–Hall equation. The selected area diffraction (SAED) arrangement (Fig. 6c–d) showed clear spots and strong concentric rings, indicating that the NPs are highly crystallized. Since every diffraction ring matched to a collection of lattice planes with the identical miller indices, the generated compositions could be identified as cubic phase, as shown by the XRD data demonstrating their phase purity. Additionally, verification of phase development was conducted by analyzing the lattice fringes observed in the images depicted in Fig. 6e–f. The d-spacing magnitudes of the lattice fringes were estimated to be 0.355 nm ($x = 0.0$) and 0.349 nm ($x = 0.2$).

## Magnetic properties analysis

The M–H loops of MZCF NPs are represented in Fig. 7. The saturation magnetization ($M_s$), remanent magnetization ($M_r$), coercive field ($H_c$), and squareness ratio ($S$) are computed and given in Table 3. The magnetic possessions of a material are influenced by both intrinsic (such as cation distribution, lattice strain, and lattice parameter) and extrinsic (such as structure, density, and manufacturing method) variables [34]. The results of this study show that all of the samples have narrow M–H loops. This could be clarified via the magnetic moments of each cation, which cause the soft magnetic behavior that is seen. According to the data presented in Fig. 7, it can be inferred that the produced ferrites exhibit ferrimagnetic properties at ambient temperature. Figure 8 illustrates the relationship between the $M_s$ and $M_r$ values and the concentration of copper ions. Evidently, as the copper (Cu)

J Mater Sci (2024) 59:4167–4185
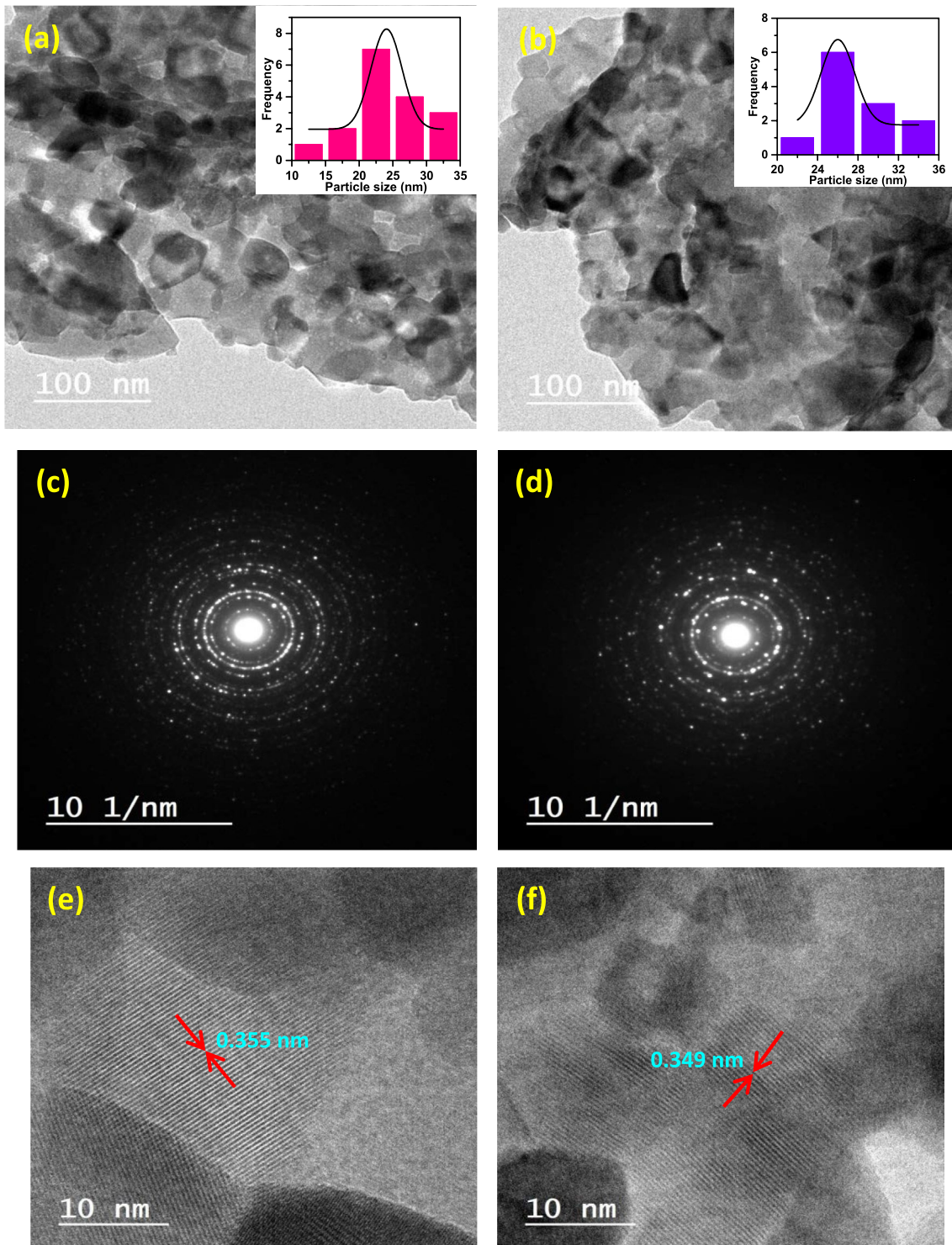


**Figure 6** **a–b** TEM images, **c–d** SAED pattern, **e–f** HRTEM lattice fringes of $Mn_{0.4}Zn_{0.6}Fe_2O_4$ and $Mn_{0.4}Zn_{0.4}Cu_{0.2}Fe_2O_4$ nanoferrites.

content progressively rises from 0.0 to 0.4, the values of $M_s$ and $M_r$ exhibit a significant increment from 40.21 to 58.78 emu/g and from 4.46 to 10.54 emu/g,

respectively. The observed improvements can be elucidated through Neel's theory [35], which posits that the cations occupying octahedral and tetrahedral
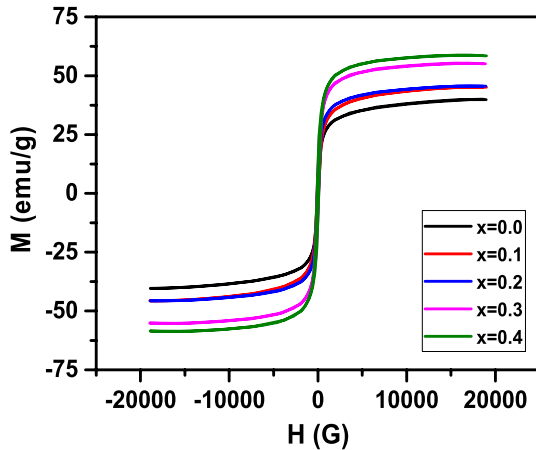
**Figure 7** M–H hysteresis loops for the MZCF nanoparticles.

sublattices exhibit opposing magnetic moments that align with each other. The resultant net magnetic moment, denoted as $\mu_{th}$, is calculated by, $\mu_{th} = |\mu_B - \mu_A|$, where $(\mu_B)$ and $(\mu_A)$ are the magnetic moments of the cations at B- and A-sites. By employing Neel's theory and taking into account the magnetic moments of $Cu^{2+}$ (1 $\mu_B$), $Zn^{2+}$ (0 $\mu_B$), $Fe^{3+}$ (5 $\mu_B$), and $Mn^{2+}$ (5 $\mu_B$), it is observed that spinel ferrites exhibit three potential interactions. The first interaction, denoted as A–O–A, is followed by the second interaction, referred to as A–O–B, and the third interaction, designated as B–O–B. Among the three exchanges being considered, it is consistently seen that the A–O–B interaction has a dominant influence and plays a crucial part in determining the magnetic characteristics shown by materials. The observed increase in $M_r$ and $M_s$ values may be caused by the increased strength of the interaction between entities A–O–B [36–38]. For MZCF, $Cu^{2+}$ ions substitute the nonmagnetic $Zn^{2+}$ ions at the B-sites. This substitution generates more unpaired electrons and enhancing the magnetic moment of B-sites. This improvement in the magnetic moment becomes the dominant factor in the A–O–B interaction. Hence, as the substitution quantity increases, both $M_s$ and $M_r$ exhibit a corresponding rise. Another factor can be

elucidated by the occurrence of the size effect. The introduction of Cu results in an augmentation of the crystallite size of MZCF. As a consequence, there is an augmentation in magnetization due to an elevation in the magnetic ordering. In an alternative approach, the equation that can be employed to compute the experimental magnetic moment is provided as follows [32]:

$$\mu_{exp} = \frac{M_{wt} \times M_s}{5585} \tag{13}$$

The value "5585" corresponds to the magnetic factor. Table 3 lists the magnetic moments that have been determined. The magnetic moment exhibits an increase from 1.71 $\mu_B$ to 2.49 $\mu_B$. This phenomenon can be attributed to the direct dependence of $\mu_{exp}$ on saturation magnetization. Based on the derived values, it can be noticed that the nanoferrites that were synthesized have favorable characteristics for utilization in high-frequency applications.

The squareness ratio ($S$) of the substance is contingent upon its anisotropy. A lower squareness ratio indicates a greater degree of isotropy in the material
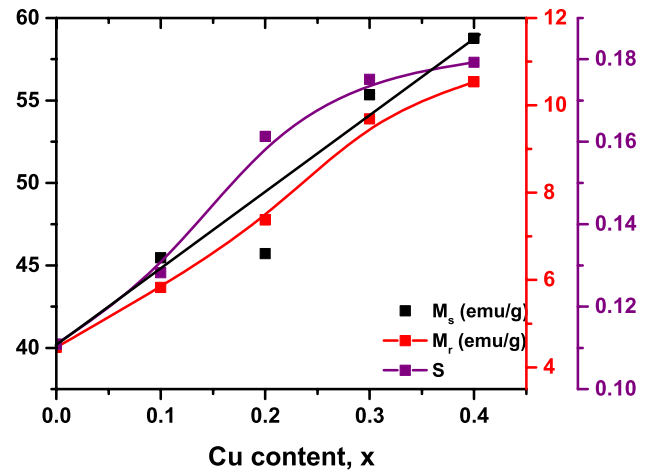


**Figure 8** Variation of remanent magnetization, saturation magnetization, and squareness ratio with copper concentration $x$.

**Table 3** The calculated magnetic parameters of MZC nanoferrites

| $x$ | $M_s$ (emu/g) | $H_c$ (G) | $M_r$ (emu/g) | $S$ | $k_1$ (erg/g) | $\mu_{exp}$ ($\mu_B$) |
|-----|---------------|-----------|---------------|-----|---------------|------------------------|
| 0.0 | 40.21 | 56.75 | 4.46 | 0.111 | 2329 | 1.706 |
| 0.1 | 45.46 | 70.55 | 5.83 | 0.128 | 3272 | 1.927 |
| 0.2 | 45.71 | 70.46 | 7.37 | 0.161 | 3287 | 1.936 |
| 0.3 | 55.34 | 83.71 | 9.69 | 0.175 | 4727 | 2.342 |
| 0.4 | 58.78 | 93.26 | 10.54 | 0.179 | 5593 | 2.485 |

[39]. The equation that is utilized for computing the squareness ratio is provided as follows:

$$S = \frac{M_r}{M_s} \qquad (14)$$

The squareness ratio rises from 0.11 to 0.18 with increased copper content. As presented in Fig. 8, the observed $S$ value is below the theoretical maximum limit 0.5. This observation suggests the presence of a disordered arrangement of spherical particles exhibiting multi-magnetic domain (MMD) behavior [40] and discloses the magnetostatic interaction between the NPs [41]. Materials with a high squareness ratio possess the potential to be employed in pulse power applications by operating in greater proximity to their saturation point. The squareness ratio reaches its highest value when $x$ is equal to 0.4.

The coercivity ($H_c$) of the spinel ferrite NPs emerged as a significant parameter in their magnetic properties. Figure 9 illustrates the relationship between the $H_c$ values and Cu content. A notable enhancement in coercivity is found when $Zn^{2+}$ ions are replaced with $Cu^{2+}$ ions inside the crystal lattice of the $Mn_{0.4}Zn_{0.6}Fe_2O_4$ system, as compared to the non-doped sample. Recent research inquiries have indicated that several elements, including microstrain, size distribution, magnetic domain size, magneto crystallinity, and anisotropy, influence a given composition's coercivity [42]. Firstly, in this particular situation, there is a correlation between the size of the crystallite and its coercivity. The X-ray diffraction examination indicated a reduction in the size of the crystallites at $x = 0.1$,
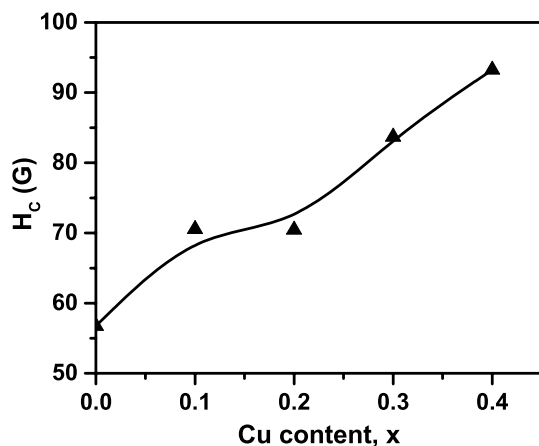
**Figure 9** The dependence of coercive field values on Cu content.

followed by an augmentation when the doping level was progressively raised. Consequently, the inclusion of $Cu^{2+}$ ions into MZCF induces the growth of larger crystallites or grains, hence causing a rise in coercivity from 56.75 to 93.26 G. Secondly, the evaluation of magnetic materials for various applications necessitates the consideration of magneto-crystalline anisotropy ($k_1$), which is a crucial performance characteristic. It can be computed based on the magnitudes of $H_c$ and $M_s$ using the following formula [43]:

$$H_c = \frac{0.98 k_1}{M_s} \qquad (15)$$

The equation demonstrates a direct correlation between the coercivity and the value of $k_1$ while indicating an inverse relationship with the value of $M_s$. The values obtained are displayed in Table 3. It has been shown that $k_1$ exhibits an upward trend when the concentration of Cu increases, leading to a subsequent increase in $H_c$. The observed rise in MZCF samples might be assigned to amplifying strong spin–orbit coupling inside the octahedral sites. The findings observed in the current study have exhibited a comparable pattern to the outcomes documented by Sikder et al. and Gilani et al. [44, 45]

Moreover, to comprehend $k_1$ of the MZCF, the magnetization results obtained at elevated magnetic fields are subjected to fitting analysis utilizing the law of approach (L. A.) to saturation as expressed by [46],

$$M = M_s \left[ 1 - \frac{a}{H} - \frac{b}{H^2} \right] - k_1 H \qquad (16)$$

The parameter $\frac{a}{H}$ is influenced by the presence of inhomogeneities within the samples, such as gaps, weakened ferromagnetic or nonferromagnetic phases, and local deformations in the crystal structure. These factors result in an uneven distribution of magnetization within the crystal, thereby impeding its attainment of saturation. On the other hand, the term $\frac{b}{H^2}$ represents the contribution of magneto-crystalline anisotropy (MCA) [47], and $k_1 H$ is referred to the forced magnetization. The phenomenon of forced magnetization arises due to a linear augmentation of the spontaneous magnetization, particularly when subjected to strong magnetic fields. The two components, namely inhomogeneity and magneto-crystalline anisotropy, are examined individually. Given that the dominating factor at higher temperatures
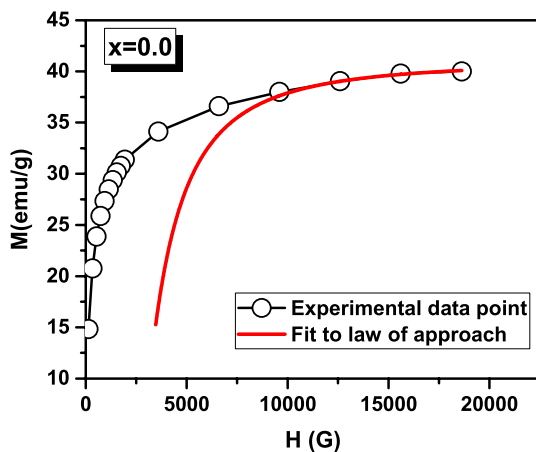
is the forced magnetization ($k_1H$), we can disregard it in our study as we specifically examined the present specimens at ambient temperature. Hence, the parameters $M_s$ and $k_1$ are the sole remaining fitting parameters in the aforementioned equation. Therefore, by excluding the forced magnetization term, the linear approximation (LA) to saturation can be expressed using the subsequent equation:

$$M = M_s \left[ 1 - \frac{b}{H^2} \right] \tag{17}$$

The calculation of the MCA constant, which is dependent on $b$, is determined by the following relationship [46]:

$$b = \frac{8k_1^2}{105\mu_o^2 M_s^2} \tag{18}$$

In this context, the symbol $\mu_0$ represents the permeability of free space. The cubic anisotropy of random polycrystalline specimens is characterized by a numerical coefficient of 8/105. Figure 10 represents L. A. to saturation fitted hysteresis curve for the MZF sample ($x = 0.0$). In order to determine the anisotropy constant ($k_1$), magnetic fields of larger magnitude are employed close to $M_s$. The magnitudes of the magnetic saturation ($M_s$) and the constant ($b$) were determined by the use of a nonlinear fitting technique on the hysteresis plot.

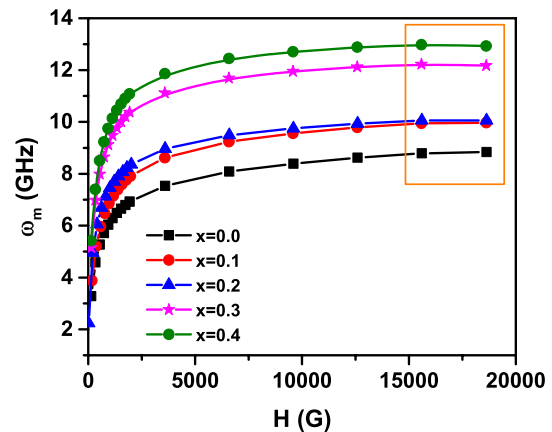## High-frequency (HF) response of MZC nano ferrites

MZC nanoferrites are applicable in HF microwave devices and several related uses. Hence, in order to observe the characteristics of NPs inside the microwave range, the microwave frequency denoted as '$\omega_m$' was determined by employing the subsequent equation [48];

$$\omega_m = 8\gamma\pi^2 M_s \tag{19}$$

The gyromagnetic ratio, denoted as $\gamma$, equals 2.8 MHz/Oe [49, 50]. Figure 11 illustrates the responsiveness of Mn–Zn nanoferrite with frequency. It has been observed that the presence of copper (Cu) in the ferrite material improves its responsiveness, making it suitable for applications in higher frequency ranges. Nevertheless, it was noted that all of the nanoferrites doped with Cu were functional at the frequencies between 8 and 13 GHz. The relationship between the size of the devices, the qualities of the materials, and the range of frequencies applied was observed. Moreover, utilizing Cu-doped Mn–Zn nanoferrites for promising applications, including magnetic memory gadgets, inductors, filters, transformer cores, and the X-band frequency domain is highly advised.

## Switching field distribution (SFD) response of MZCF

The analysis of the SFD involved the utilization of the first derivative of the demagnetization plots for MZCF NPs [51] as illustrated in Fig. 12. The observed results provide evidence of the exchange coupling



**Figure 10** Representative fitted curve of magnetization for MZF calculated by LA.



**Figure 11** Microwave high frequency response of the Cu-doped MnZn nanoferrites.
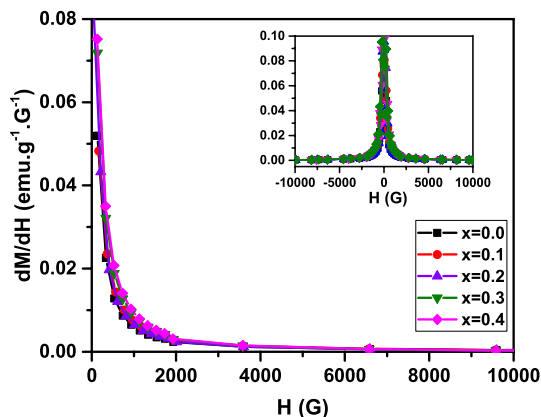
**Figure 12** SFD response of MZC nanoferrites.



**Figure 13** Percent diffuse reflectance vs wavelength spectra of all MZC nanoferrites.
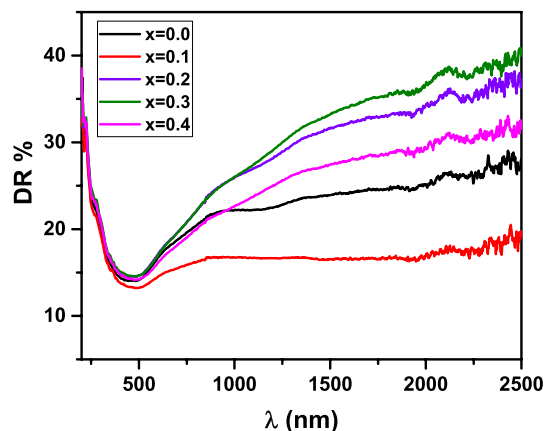
interactions among the metal cations at their respective lattice positions. The obtained SFD curves indicated a reduction in *dM/dH*. Cation–cation interactions inside the spinel lattice are responsible for the observed effects [52]. The Mn–Zn ferrite doped with Cu exhibited a greater response when subjected to a strong reverse field, while the curves were more uniform at high field intensities. This phenomenon can be ascribed to the significant interactions among cations at higher reverse field conditions. The Mn–Zn ferrite exhibited a weakened SFD response, but the Mn–Zn ferrite doped with copper had a more pronounced SFD response. Furthermore, the curve clarified in the inset of Fig. 12 has a solitary peak. The narrowness of the observed peak serves as evidence for the confirmation of a confined magnetic domain distribution. The observation of a peak in close proximity to the zero point of the magnetic field serves as empirical support for the inherent soft magnetic properties shown by the NPs.

## UV–visible analysis

Scientists and researchers have been engaged in the development of specialized nanoferrites for optoelectronic devices in order to produce the most efficient magnetic materials. This is primarily driven by the favorable characteristics of spinel ferrites, such as their significant surface–volume ratio and the high dimensionality of their nanoparticles. Figure 13 illustrates the spectrum of DR% for nanoparticles of $Mn_{0.4}Zn_{0.6-x}Cu_xFe_2O_4$, where *x* values range from 0.0 to 0.4. The spectra exhibited reflectance intensities ranging from 14 to 33% within the wavelength range of

200–500 nm, after which there was a further rise up to a supreme value for the remaining range of wavelengths. The Kubelka–Munk (K–M) technique was utilized to assess the reflectance function, denoted as $F(R)$, in the study [53]:

$$F(R) = \frac{\alpha}{S} = \frac{(1-R)^2}{2R} \tag{20}$$

where $\alpha$ and $S$ represent the molar absorption and scattering coefficients. Various methodologies have been employed to assess the optical band gap of NPs, with Tauc's relation [54] being the predominant and widely utilized way. It is stated as follows:

$$F(R)h\upsilon = A\left(h\upsilon - E_g\right)^n \tag{21}$$

In the given expression, the symbol '*h*' gives Planck's constant, '*v*' indicates the frequency, '*A*' corresponds to the constant that relies on the transition, '$E_g$' signifies the band gap energy, and '*n*' is an index that denotes the kind of transitions. The index '*n*' corresponds to the values 1/2 and 2, representing direct allowed, and indirect allowed transitions, respectively. Subsequently, by the process of extending the linear segment of the graph depicting the relationship between $(F(R)h\upsilon)^{1/n}$ versus $h\upsilon$, specifically at the point where $(F(R)h\upsilon)^{1/n}$ equals zero, it becomes feasible to get the precise measurement of the band gap energy ($E_g$). In order to determine the energy gap of MZC nanoferrites, several values of n were examined. Ultimately, it was determined that the optimal value for *n* is ½, indicating that the researched nanoferrites

possess a direct permitted energy gap. Figure 14 illustrates Tauc's graphs for every specimen of MZC nanoferrites. The direct band gap values for a pure MZ ferrite sample are measured to be 1.78 eV. For MZF samples doped with copper, the range of direct band gap values observed is between 1.61 and 1.72 eV. The semiconducting characteristics of the produced ferrites are apparent based on the obtained values. In a study performed by Almessiere et al., it was shown that the mixed spinel MZF had an $E_g$ value of 1.64 eV [55]. Nevertheless, there is a lack of documented empirical evidence on MZCF in existing academic research. Table 4 presents the optical band gap of the Cu-substituted MZ nanoferrites. The energy band gap of nanoferrites is influenced by several factors. These factors encompass the interstitial oxygen vacancies, size of nano-crystallites, roughness of the surface, and the presence of mixed cations at the two locations [56]. The behavior of the $E_g$ values is interpreted depending on the role of Cu and the size of the particles. The band gap energies of particles are determined by several

**Table 4** Optical band gap and kinetic parameters of photocatalytic degradation of MB dye with synthesized NPs

| $x$ | $E_g$ (eV) | $K_1$ (min$^{-1}$) | $R^2$ |
|-----|-----------|---------------------|-------|
| 0.0 | 1.78 | 0.0037 | 0.971 |
| 0.1 | 1.61 | – | – |
| 0.2 | 1.72 | – | – |
| 0.3 | 1.7 | – | – |
| 0.4 | 1.65 | 0.0032 | 0.933 |

factors, including as particle size, shape, and type. Smaller particles have a larger band gap, resulting in their absorption of light with higher energy [57]. Introducing additional cations into the structural lattice modifies the energy levels, leading to the development of sub-bands through the overlapping of O-2p and Fe-3d levels. The generation of sub-band gap energy levels enables the transitions between the VB and CB, leading to a decrease in the $E_g$ values for $x \geq 0.1$. Furthermore, the decline in the band gap energy ($E_g$) in
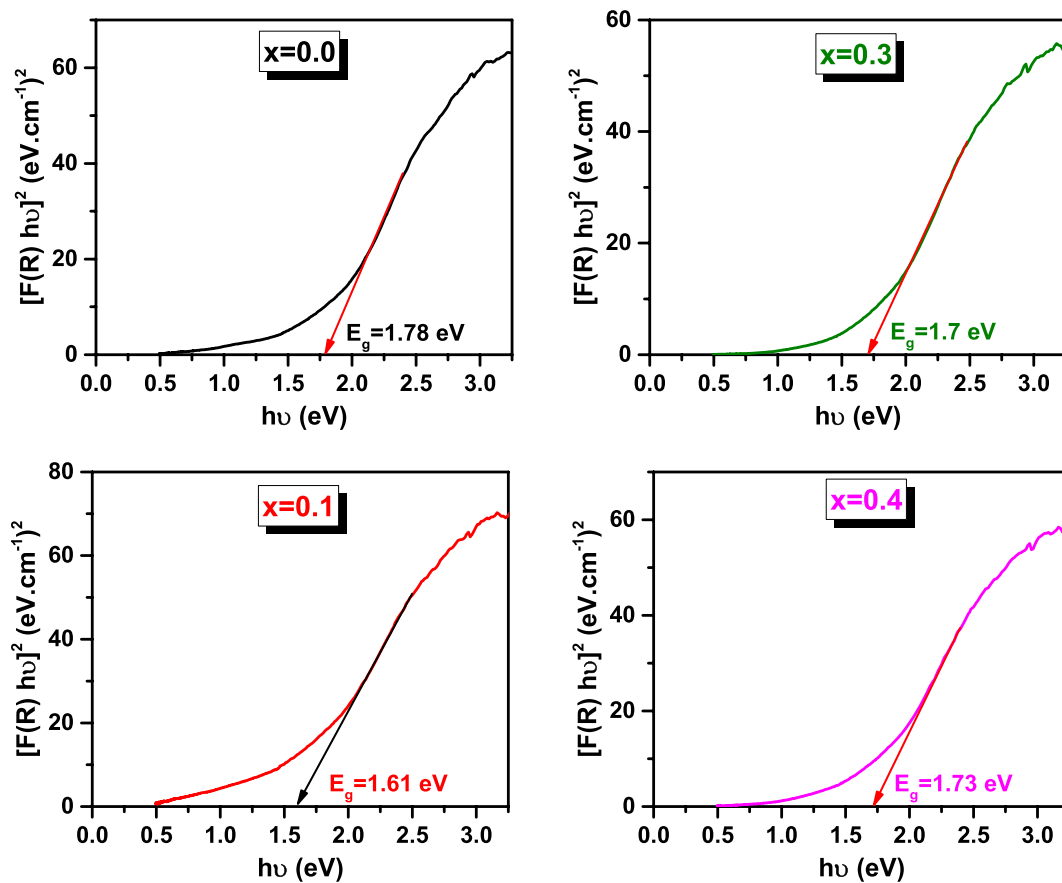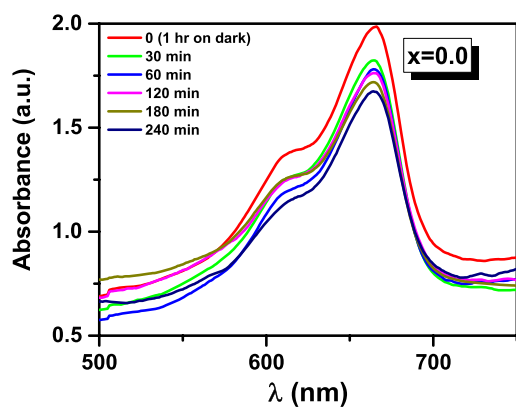


**Figure 14** Tauc plots of Cu-doped Mn–Zn ($x = 0.00$, 0.1, 0.3, and 0.4) nanoferrites.

our samples might be linked to the reduction in the lattice constant and unit cell volume, which indicates structural modifications resulting from the addition of Cu to MZF nanoparticles. The band gap refers to the amount of energy required for an electron to transition from the VB to the CB. This transition allows the electron to move freely within the crystal lattice and act as a charge carrier for the conduction of electric current. Therefore, the band gaps of the ferrite materials play a crucial role in enabling the devices to function well at high temperatures in typical circumstances. These characteristics render them very appealing for a wide range of possible uses. Furthermore, it is worth noting that produced samples within the range of $x = 0.0–0.4$ exhibit optical absorption properties below 650 nm, making them potentially suitable for use in photocatalytic applications.

## Photocatalytic activity

Photocatalysis has gained recognition as a highly efficient and suitable manner for the elimination of organic pollutants from aqueous solutions due to its environmentally benign characteristics, exceptional removal efficacy, cost-effectiveness, and enhanced water reusability. In order to examine the PCD of MZCF, the produced photocatalyst was used to destroy MB dye. A solar simulator was used to measure the PCD of the mixtures for a full 240 min, with readings made every 30 min. Figure 15 illustrates the absorbance of MB dye when added $Mn_{0.4}Zn_{0.6}Fe_2O_4$ ($x = 0.0$) and $Mn_{0.4}Zn_{0.2}Cu_{0.4}Fe_2O_4$ ($x = 0.4$) photocatalysts. Degradation of MB dye is sped up in the presence of a catalyst, as seen by a decrease in absorbance at 664 nm, which corresponds to the dye's characteristic absorbance peak.
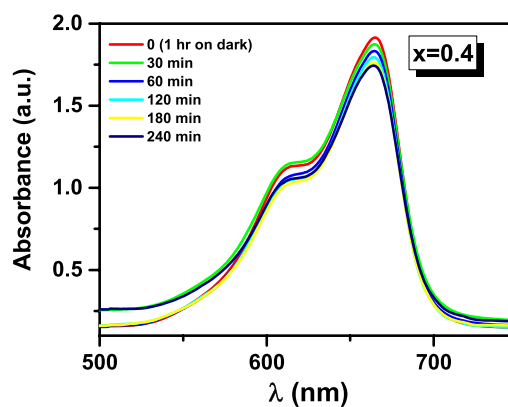
The formula used for the determination of the degree of degradation efficiency (DE%) is as follows:

$$DE\% = \frac{C_o - C_t}{C_o} \times 100 \tag{22}$$

Dye concentrations before and after being exposed to light are denoted by $C_0$ and $C_t$, respectively. The degradation of dye over a period of 240 min is assessed for two different copper concentrations, namely $x = 0.0$ and $x = 0.4$. The resulting degradation percentage of dye in the water were determined to be 16 and 9%, respectively. Figure 16 illustrates the observed variability in degradation efficiency. The potential explanation for the higher photocatalytic activity observed in the MZF sample compared to the MZCF sample might be attributed to a decrease in crystallite size [58].
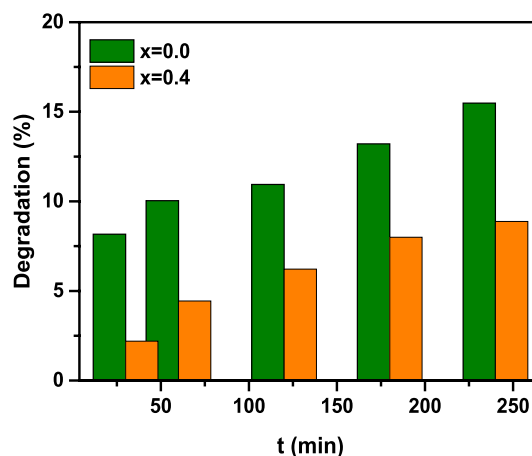


Figure 16 Graph representing percentage degradation concerning the time of MB using prepared photocatalysts.



Figure 15 UV–Vis absorption spectra of MB using $Mn_{0.4}Zn_{0.6}Fe_2O_4$ and $Mn_{0.4}Zn_{0.2}Cu_{0.4}Fe_2O_4$.

## Degradation kinetics

The rate of MB dye elimination over photocatalysts was determined by the Langmuir Hinshelwood kinetic concept [59, 60]:

$$\ln\left(\frac{C_t}{C_o}\right) = K_1 t \qquad (23)$$

The symbol $K_1$ denotes the constant rate value associated with the photo-degradation process. Figure 17 displays the plot of the first-order reaction for MB, specifically $\ln(C_0/C_t)$ against time ($t$). The rate constant for the reaction may be estimated by fitting a linear equation to the points acquired from the graph and calculating the slope of the resultant linear line. Furthermore, it is worth noting that the degree of fit to the model increases as the value of the correction coefficient ($R^2$) increases. This coefficient serves as a significant criterion for evaluating the fit of the calculated points on the curve. Table 4
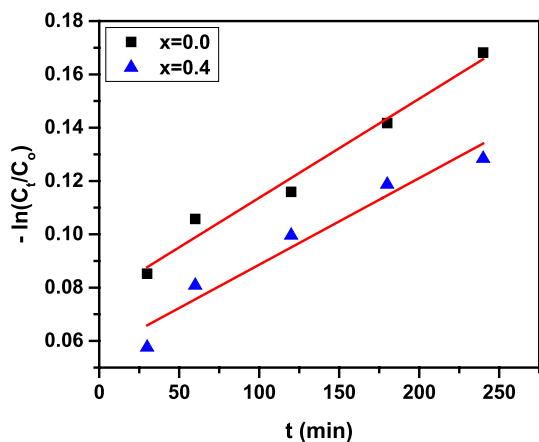


**Figure 17** Pseudo-first-order kinetics of MB dye using $Mn_{0.4}Zn_{0.6-x}Cu_x Fe_2O_4$ ($x = 0.0$, and 0.4) as a photocatalyst.
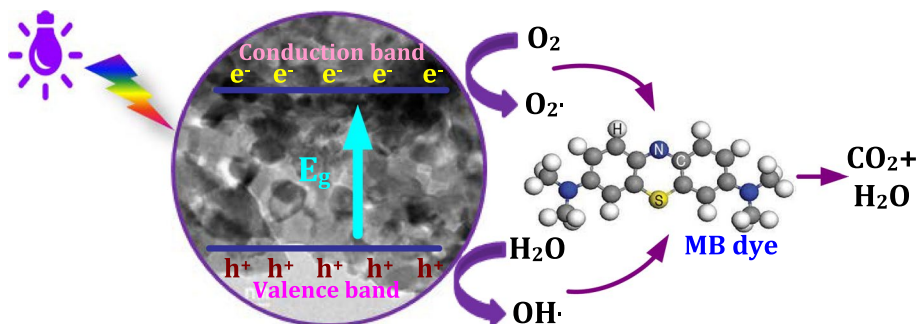
displays the estimated rate constants and $R^2$ values for various catalyst concentrations based on these plots.

## Photocatalytic mechanism

Figure 18 illustrates the whole process of how the photocatalytic procedure works. When an aqueous solution containing the nanoferrite catalyst is exposed to light with higher band gap energy than that of ferrites, electron–hole pairs are produced in the conduction band. A portion of the electron–hole pairs undergo recombination with the majority of the semiconductor, while others migrate to the catalyst's surface. At the surface, both the holes and electrons function as potent oxidizing agents. The catalyst site facilitates the occurrence of a process whereby the photogenerated electrons interact with adsorbed molecule $O_2$, resulting in its reduction to the superoxide radical anion $O_2^-$. Conversely, the dye molecules undergo direct oxidation under the action of photogenerated holes. These holes might play a role in the generation of hydroxyl radicals (OH·) by facilitating the oxidation of $OH^-$ ions and $H_2O$ molecules adsorbed on the catalyst's surface. These OH· exhibit strong oxidizing properties. By starting the breakdown of the bound molecule close to the surface of the catalyst, these processes could lead to the full mineralization of organic molecules. In the context of photocatalytic activity involving oxidation, there are two distinct mechanisms for the generation of OH·. Electrons are excited from the valence band to the conduction band when light energy is supplied to the ferrite catalyst, creating electron–hole pairs [61–63]. The following reactions show that the photogenerated holes are ultimately responsible for the formation of OH·:

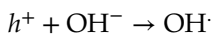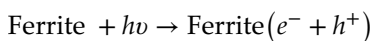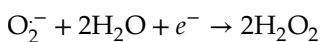$$Ferrite + hv \rightarrow Ferrite(e^- + h^+)$$

$$h^+ + OH^- \rightarrow OH·$$
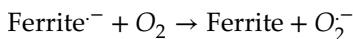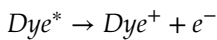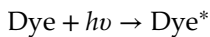


**Figure 18** Band structure and possible photocatalytic mechanism.

Additionally, the dye molecules show visible-light absorption, which results in a migration of photogenerated electrons from the dye molecule to the ferrite surface. The reactions that are involved include:

$$Dye + h\nu \rightarrow Dye^*$$

$$Dye^* \rightarrow Dye^+ + e^-$$

$$Ferrite + e^- \rightarrow Ferrite^- \rightarrow Ferrite^{\cdot-}$$

$$Ferrite^{\cdot-} + O_2 \rightarrow Ferrite + O_2^{\cdot-}$$

$$O_2^- + 2H_2O + e^- \rightarrow 2H_2O_2$$

$$H_2O_2 + e^- \rightarrow .OH + OH^-$$
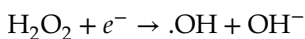
The generation of active OH· results in the breakdown of the dye molecule:

$$Dye^{\cdot+} + OH^- \rightarrow \text{degraded products}$$
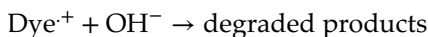
Therefore, the use of visible light for dye degradation proves to be a highly efficient method that has no detrimental consequences to the environment, ultimately yielding carbon dioxide ($CO_2$) and water ($H_2O$) as the ultimate by-products of degradation.

## Conclusion

$Mn_{0.4}Zn_{0.6-x}Cu_xFe_2O_4$ nanoferrites were successfully synthesized using the citrate technique, with varying values of $x$ (0, 0.1, 0.2, 0.3, and 0.4). X-ray diffraction (XRD) research was employed to confirm the presence of a cubic phase within a monophasic structure. The increase in copper content resulted in a rise in both bulk and X-ray densities. The use of copper (Cu) as a dopant in manganese–zinc nanoferrites resulted in the augmentation of their magnetic properties. The determination of the MCA constant has been performed utilizing the L. A. formalism. The examination encompassed an analysis of both high frequency and steady-state frequency response. The research results revealed that MZCF demonstrated a more pronounced magnetic response, suggesting its potential appropriateness for applications related to switching and high-frequency microwave absorption requirements. The energy gap of MZCF nanoparticles was calculated and seen to vary between 1.61 and 1.78 (eV). The

assessment of photocatalytic degradation efficiency was conducted using the generated samples.

## Data and code availability

Data supporting the findings of the current study are available from the corresponding authors upon request.

## Declarations

**Conflict of interest** The authors declare that they have no known competing financial interests or personal relationships that could have appeared to influence the work reported in this paper.

## References

[1] Sudheesh VD, Thomas N, Roona N, Choudhary H, Sahoo B, Lakshmi N, Sebastian V (2018) Synthesis of nanocrystalline spinel ferrite ($MFe_2O_4$, M= Zn and Mg) by solution combustion method: influence of fuel to oxidizer ratio. J Alloys Compd 742:577–586

[2] Shirsath SE, Kadam RH, Gaikwad AS, Ghasemi A, Morisako A (2011) Effect of sintering temperature and the particle size on the structural and magnetic properties of nanocrystalline $Li_{0.5}Fe_{2.5}O_4$. J Magn Magn Mater 323:3104–3108.

[3] Zhang Y, Wang M, Chang C, Xu K, Ma H, Zhao F (2018) A DFT study on the enthalpies of thermite reactions and enthalpies of formation of metal composite oxide. Chem Phys 507:19–27

[4] Zhang CF, Zhong XC, Yu HY, Liu ZW, Zeng DC (2009) Effects of cobalt doping on the microstructure and magnetic properties of Mn–Zn ferrites prepared by the co-precipitation method. Phys B Condens Matter 404:2327–2331

[5] Zheng Y, Jia L, Xu F, Wang G, Shi X, Zhang H (2019) Microstructures and magnetic properties of low temparature sintering NiCuZn ferrite ceramics for microwave applications. Ceram Int 45:22163–22168

[6] Goldman A (2006) Modern ferrite technology. Springer, Cham

[7] Rehman AU, Morley NA, Amin N, Arshad MI, un Nabi MA, Mahmood K, Ali A, Aslam A, Bibi A, Iqbal MZ (2020) Controllable synthesis of $La^{3+}$-doped $Zn_{0.5}Co_{0.25}Cu_{0.2}5Fe_{2-x}La_xO_4$ (x= 0.0, 0.0125, 0.025, 0.0375, 0.05) nano-ferrites by sol-gel auto-combustion route. Ceram Int 46:29297–29308.

[8] Abu-Elsaad NI, Nawara AS, Mazen SA (2020) Synthesis, structural characterization, and magnetic properties of Ni–Zn nanoferrites substituted with different metal ions ($Mn^{2+}$, $Co^{2+}$, and $Cu^{2+}$). J Phys Chem Solids, 109620.

[9] Woltz S, Hiergeist R, Görnert P, Rüssel C (2006) Magnetite nanoparticles prepared by the glass crystallization method and their physical properties. J Magn Magn Mater 298:7–13

[10] Mazen SA, Abu-Elsaad NI (2010) Analogous study in low magnetic field between Cu-Ge and Cu-Si ferrites. J Magn Magn Mater, p 322. https://doi.org/10.1016/j.jmmm.2009.09.029.

[11] Abu-Elsaad NI, Mazen SA, Kumar ER (2024) Structural, vibrational and magnetic properties of heat treated $CuFe_2O_4$ nanoparticles prepared by two different synthesis routes. Ceram Int 50:3693–3700. https://doi.org/10.1016/j.ceramint.2023.11.121.

[12] Melo RS, Silva FC, Moura KRM, De Menezes AS, Sinfrônio FSM (2015) Magnetic ferrites synthesised using the microwave-hydrothermal method. J Magn Magn Mater 381:109–115

[13] Akhtar MN, Sulong AB, Akhtar MN, Khan MA (2018) Systematic study of $Ce^{3+}$ on the structural and magnetic properties of Cu nanosized ferrites for potential applications. J Rare Earths 36:156–164

[14] Zimbone M, Cacciato G, Sanz R, Carles R, Gulino A, Privitera V, Grimaldi MG (2016) Black TiOx photocatalyst obtained by laser irradiation in water. Catal Commun 84:11–15

[15] Marimuthu S, Antonisamy AJ, Malayandi S, Rajendran K, Tsai P-C, Pugazhendhi A, Ponnusamy VK (2020) Silver nanoparticles in dye effluent treatment: a review on synthesis, treatment methods, mechanisms, photocatalytic degradation, toxic effects and mitigation of toxicity. J Photochem Photobiol B Biol 205:111823

[16] Okello C, Tomasello B, Greggio N, Wambiji N, Antonellini M (2015) Impact of population growth and climate change on the freshwater resources of Lamu Island, Kenya. Water 7:1264–1290

[17] Dhiman P, Rana G, Kumar A, Sharma G, Vo D-VN, AlGarni TS, Naushad M, ALOthman ZA (2021) Nanostructured magnetic inverse spinel Ni–Zn ferrite as environmental friendly visible light driven photo-degradation of levofloxacin. Chem Eng Res Des 175:85–101.

[18] Bagade AV, Pund SN, Nagwade PA, Kumar B, Deshmukh SU, Kanagare AB (2023) Ni-doped Mg-Zn nano-ferrites: Fabrication, characterization, and visible-light-driven photocatalytic degradation of model textile dyes. Catal Commun, 106719.

[19] Chahar D, Taneja S, Bisht S, Kesarwani S, Thakur P, Thakur A, Sharma PB (2021) Photocatalytic activity of cobalt substituted zinc ferrite for the degradation of methylene blue dye under visible light irradiation. J Alloys Compd 851:156878

[20] Ramadevi P, Shanmugavadivu R, Venkatesan R, Mayandi J, Sagadevan S (2023) Photocatalytic dye degradation efficiency and reusability of aluminium substituted nickel ferrite nanostructures for wastewater remediation. Inorg Chem Commun 150:110532

[21] Abu-Elsaad NI, Mazen SA, Nawara AS (2022) Impact of erbium on structural, optical, magnetic and photocatalytic performance of Co-Mn nanoferrites. Phys Scr 97:125801

[22] Mahmood A, Maqsood A (2023) High-frequency dielectric response of 3d metal (Mn and Cu) doped zinc ferrite nanoparticles for microwave applications. Mater Today Commun 34:105042

[23] Alam F, Rahman ML, Das BC, Hossain AKMA (2020) Effect of $Cu^{2+}$ on structural, elastic and magnetic properties of nanostructured Mn–Zn ferrite prepared by a sol-gel auto-combustion method. Phys B Condens Matter 594:412329

[24] Mazen SA, Elsayed HM, Abu-Elsaad NI (2020) Effect of divalent metal ions substitution on structural and magnetic properties of $Li_{0.25}Mn_{0.5-x}M_xFe_{2.25}O_4$ (M= $Co^{2+}$, $Ni^{2+}$, $Cu^{2+}$) spinel ferrites. Mater Chem Phys 256:123676.

[25] Cullity BD (1956)Elements of X-ray diffraction. Addison-Wesley Publishing, Boston.

[26] Luo G, Zhou W, Jian-de LI, Jiang G, Tang S, Du Y (2015) Effect of Cu ion substitution on structural and dielectric properties of Ni–Zn ferrites. Trans Nonferrous Met Soc China 25:3678–3684

[27] Williamson GK, Hall WH (1953) X-ray line broadening from filed aluminium and wolfram. Acta Metall 1:22–31

[28] Abu-Elsaad NI, Mazen SA, Sleem AY (2022) Production of $Cr^{3+}$ substituted Li–Zn nanocrystalline ferrite by citrate method: Studies on structure, cation occupancy, elastic, optical and magnetic performance. Ceram Int 48:14210–14223. https://doi.org/10.1016/j.ceramint.2022.01.309

[29] Standely J (1972) Oxide magnetic materials. Clarendon, Oxford.

[30] Tatarchuk TR, Bououdina M, Paliychuk ND, Yaremiy IP, Moklyak VV (2017) Structural characterization and anti-structure modeling of cobalt-substituted zinc ferrites. J Alloys Compd 694:777–791

[31] Arean CO, Diaz EG, Gonzalez JMR, Garcia MAV (1988) Crystal chemistry of cadmium-zinc ferrites. J Solid State Chem 77:275–280

[32] Smit J, Wijn HPJ (1959) Ferrites, Philips technical library. Eindhoven, The Netherlands, p 278.

[33] Kumar G, Kotnala RK, Shah J, Kumar V, Kumar A, Dhiman P, Singh M (2017) Cation distribution: a key to ascertain the magnetic interactions in a cobalt substituted Mg–Mn nanoferrite matrix. Phys Chem Chem Phys 19:16669–16680

[34] Akhtar MN, Khan MA (2018) Effect of rare earth doping on the structural and magnetic features of nanocrystalline spinel ferrites prepared via sol gel route. J Magn Magn Mater 460:268–277

[35] Néel L (1948) Propriétés magnétiques des ferrites; ferrimagnétisme et antiferromagnétisme. Ann Phys (Paris), pp 137–198.

[36] Venkataraju C, Sathishkumar G, Sivakumar K (2011) Effect of Cd on the structural, magnetic and electrical properties of nanostructured Mn–Zn ferrite. J Magn Magn Mater 323:1817–1822

[37] Slama J, Grusková A, Ušáková M, Ušák E, Dosoudil R (2009) Contribution to analysis of Cu-substituted NiZn ferrites. J Magn Magn Mater 321:3346–3351

[38] Mazen S, Abu-Elsaad NI, Nawara AS (2020) The Influence of Various Divalent Metal Ions ($Mn^{2+}$, $Co^{2+}$, and $Cu^{2+}$) Substitution on the Structural and Magnetic Properties of Nickel-Zinc Spinel Ferrite. Phys Solid State 62:1183–1194

[39] Smart JS (1955) The Néel theory of ferrimagnetism. Am J Phys 23:356–370

[40] Almessiere MA, Slimani Y, Sertkol M, Nawaz M, Sadaqat A, Baykal A, Ercan I, Ozçelik B (2019) Effect of $Nb^{3+}$ substitution on the structural, magnetic, and optical properties of $Co_{0.5}Ni_{0.5}Fe_2O_4$ nanoparticles. Nanomaterials 9:430.

[41] El-Bassuony AAH, Abdelsalam HK (2020) Synthesis, characterization, magnetic and antimicrobial properties of silver chromite nanoparticles. J Mater Sci Mater Electron 31:3662–3673

[42] Panda RK, Muduli R, Behera D (2015) Electric and magnetic properties of Bi substituted cobalt ferrite nanoparticles: evolution of grain effect. J Alloys Compd 634:239–245

[43] Mane DR, Birajdar DD, Shirsath SE, Telugu RA, Kadam RH (2010) Structural and magnetic characterizations of Mn-Ni-Zn ferrite nanoparticles. Phys Status Solidi 207:2355–2363

[44] Sikder MS, Hossain MD, Sardar I, Hossain MS, Khan MNI, Rahman MR (2023) Improved magnetic and dielectric quality factors with low losses in rare earth (Eu) substituted Co-Ni-Zn ferrites for high frequency devices. Results Phys 46:106320

[45] Gilani ZA, Khalid M, Hussain G, Shar MA, Ali SM, Khan MA, Sheikh FA, Alhazaa A (2023) Impact of cerium substitution cobalt–zinc spinel ferrites for the applications of high frequency devices. Phys B Condens Matter 660:414873

[46] Herbst JF, Pinkerton FE (1998) Law of approach to saturation for polycrystalline ferromagnets: Remanent initial state. Phys Rev B 57:10733

[47] Devi EC, Soibam I (2019) Law of approach to saturation in Mn–Zn ferrite nanoparticles. J Supercond Nov Magn 32:1293–1298

[48] Akhtar MN, Saleem M, Khan MA (2018) Al doped spinel and garnet nanostructured ferrites for microwave frequency C and X-band applications. J Phys Chem Solids 123:260–265

[49] Majeed A, Khan MA, ur Raheem F, Hussain A, Iqbal F, Murtaza G, Akhtar MN, Shakir I, Warsi WF (2016) Structural elucidation and magnetic behavior evaluation of rare earth (La, Nd, Gd, Tb, Dy) doped BaCoNi-X hexagonal nano-sized ferrites. J Magn Magn Mater 408:147–151.

[50] Gaba S, Kumar A, Rana PS, Arora M (2018) Influence of $La^{3+}$ ion doping on physical properties of magnesium nanoferrites for microwave absorption application. J Magn Magn Mater 460:69–77

[51] Panagiotopoulos I, Withanawasam L, Hadjipanayis GC (1996) 'Exchange spring' behavior in nanocomposite hard magnetic materials. J Magn Magn Mater 152:353–358

[52] Akhtar MN, Ali K, Umer A, Ahmad T, Khan MA (2018) Structural elucidation, and morphological and magnetic behavior evaluations, of low-temperature sintered, Ce-doped, nanostructured garnet ferrites. Mater Res Bull 101:48–55

[53] López R, Gómez R (2012) Band-gap energy estimation from diffuse reflectance measurements on sol–gel and commercial $TiO_2$: a comparative study. J Sol-Gel Sci Technol 61:1–7

[54] Tauc J (1968) Optical properties and electronic structure of amorphous Ge and Si. Mater Res Bull 3:37–46

[55] Almessiere MA, Güner S, Slimani Y, Baykal A, Shirsath SE, Korkmaz AD, Badar R, Manikandan A (2022) Investigation on the structural, optical, and magnetic features of $Dy^{3+}$ and $Y^{3+}$ co-doped $Mn_{0.5}Zn_{0.5}Fe_2O_4$ spinel ferrite nanoparticles. J Mol Struct 1248:131412.

[56] Lal G, Punia K, Dolia SN, Alvi PA, Dalela S, Kumar S (2019) Rietveld refinement, Raman, optical, dielectric, Mössbauer and magnetic characterization of superparamagnetic fcc-$CaFe_2O_4$ nanoparticles. Ceram Int 45:5837–5847

[57] Yadav RS, Kuřitka I, Vilcakova J, Urbánek P, Machovsky M, Masař M, Holek M (2017) Structural, magnetic, optical, dielectric, electrical and modulus spectroscopic characteristics of $ZnFe_2O_4$ spinel ferrite nanoparticles synthesized via honey-mediated sol-gel combustion method. J Phys Chem Solids 110:87–99

[58] Yin M, Li Z, Kou J, Zou Z (2009) Mechanism investigation of visible light-induced degradation in a heterogeneous $TiO_2$/Eosin Y/Rhodamine B system. Environ Sci Technol 43:8361–8366

[59] Fu Y, Chen H, Sun X, Wang X (2012) Combination of cobalt ferrite and graphene: high-performance and recyclable visible-light photocatalysis. Appl Catal B Environ 111:280–287

[60] Kossar S, Banu IBS, Aman N, Amiruddin R (2021) Investigation on photocatalytic degradation of crystal violet dye using bismuth ferrite nanoparticles. J Dispers Sci Technol 42:2053–2062

[61] Galindo C, Jacques P, Kalt A (2001) Photodegradation of aminoazobenzene acids orange 52 by three advanced oxidation process: UV/$TiO_2$, UV/$H_2O_2$ and Vis/$TiO_2$. J Photochem Photobiol A Chem 141:47–56

[62] Behnajady MA, Modirshahla N, Hamzavi R (2006) Kinetic study on photocatalytic degradation of CI Acid Yellow 23 by ZnO photocatalyst. J Hazard Mater 133:226–232

[63] Evgenidou E, Fytianos K, Poulios I (2005) Semiconductor-sensitized photodegradation of dichlorvos in water using $TiO_2$ and ZnO as catalysts. Appl Catal B Environ 59:81–89